

Phenomenology of Radion in Randall-Sundrum Scenario

Kingman Cheung

Department of Physics, University of California, Davis, CA 95616 USA
National Center for Theoretical Science, National Tsing Hua University,
*Hsinchu, Taiwan R.O.C. **

The success of the Randall-Sundrum scenario relies on stabilization of the modulus field or the radion, which is the scalar field about the background geometry. The stabilization mechanism proposed by Goldberger and Wise has the consequence that this radion is lighter than the graviton Kaluza-Klein states so that the first particle to be discovered is the radion. In this work, we study in details the decay, production, and detection of the radion at hadronic, e^+e^- , and $\gamma\gamma$ colliders.

I. INTRODUCTION

The standard model (SM) has been very successful in accounting for almost all experimental data. Nevertheless, the SM can only be a low energy limit of a more fundamental theory because it cannot explain a number of theoretical issues, one of which is the gauge hierarchy problem between the only two known scales in particle physics – the weak and Planck scales. This longstanding problem has been the subject of attention for a long time, such as supersymmetric and technicolor theories.

Recent advances in string theories have revolutionized our perspectives and understanding of the problems, namely, the Planck, grand unification, and string scales can be brought down to a TeV range with the help of extra dimensions, compactified or not. Arkani-Hamed *et al.* [1] proposed that using compactified dimensions of large size (as large as mm) can bring the Planck scale down to TeV range. In this model, the SM fields reside on a 3-brane while only gravity is allowed in the extra dimensions. The phenomenology is due to the Kaluza-Klein states of the graviton in the bulk. A summary of collider phenomenology can be found in Ref. [2]. Another interesting model was proposed by Dienes *et al.* [3] that with gauge fields and/or fermion fields allowed in the extra dimensions, the grand unification scale is brought down to TeV range.

Randall and Sundrum (RS) [4] proposed a 5-dimensional space-time model with a nonfactorizable metric to solve the hierarchy problem. The extra dimension is a single S^1/Z_2 orbifold, in which two 3-branes of opposite tensions reside at the two fixed points (boundaries) of the orbifold and a cosmological constant in the bulk serves as the source for 5-dimensional gravity. The resulting space-time metric is nonfactorizable and depends on the radius r_c of the extra dimension

$$ds^2 = e^{-2kr_c|\phi|} \eta_{\mu\nu} dx^\mu dx^\nu - r_c^2 d\phi^2 ,$$

where k is a parameter of order of M , the effective Planck scale of the theory, and ϕ is the coordinate for the extra dimension. The two 3-branes reside at $\phi = 0$ and $\phi = \pi$. The 4-dimensional Planck mass M_{Pl} is related to the scale M by

$$M_{\text{Pl}}^2 = \frac{M^3}{k} (1 - e^{-2kr_c\pi}) ,$$

so that M_{Pl} is of order M . Thus, a field that is confined to the 3-brane at $\phi = \pi$ with mass parameter m_0 will have a physical mass of $m_0 e^{-kr_c\pi}$. For kr_c around 12, the weak scale can be dynamically generated from the fundamental scale M .

The RS model has a four-dimensional massless scalar, the modulus or radion, about the background geometry:

$$ds^2 = e^{-2k|\phi|T(x)} g_{\mu\nu}(x) dx^\mu dx^\nu - T^2(x) d\phi^2 ,$$

*Present address.

Email address: cheung@phys.cts.nthu.edu.tw

where $g_{\mu\nu}(x)$ is the 4-dimensional graviton and $T(x)$ is the radion. The most important ingredients of the above brane configuration are the required size of the modulus field such that it generates the desired weak scale from the scale M and the stabilization of the modulus field at this value. A stabilization mechanism was proposed by Goldberger and Wise [5] that a bulk scalar field propagating in the background solution of the metric can generate a potential that can stabilize the modulus field. The minimum of the potential can be arranged to give the desired value of kr_c without fine tuning of parameters. It has been shown [6] that if a large value of $kr_c \sim 12$, needed to solve the hierarchy problem, arises from a small bulk scalar mass then the modulus potential near its minimum is nearly flat for values of modulus VEV that solves the hierarchy problem. As a consequence, besides getting a mass the modulus field is likely to be lighter than any Kaluza-Klein modes of any bulk field. The mass of the radion is of order of $O(\text{TeV})$ and the strength of coupling to the SM fields is of order of $O(1/\text{TeV})$. Therefore, the detection of this radion will be the first signature of the RS model and the stabilization mechanism by Goldberger and Wise. Furthermore, the radion has to have mass in order for a brane world (RS model here) to reproduce the ordinary 4-dimensional Einstein gravity [7].

In the present paper, we perform a comprehensive study of the decay, production, and detection and possible existing limits of the radion. Similar works have been considered in Refs. [8–10]. The improvement here includes: (i) more production channels and cross sections are studied, e.g., $p\bar{p} \rightarrow t\bar{t}\phi$ and $p\bar{p} \rightarrow W\phi, Z\phi$, (ii) we also perform background studies on selected channels and their feasibility of detection, and (iii) we check against the existing data on the Higgs boson at the Tevatron and at the LEP to see if the data can place some limits on the radion.

The organization of the paper is as follows. In the next section, we summarize the effective interactions of the radion. In Sec. III, we present the decay of the radion. In Sec. IV, we calculate the production cross sections for all relevant channels at e^+e^- , hadronic, and photon colliders. Section V consists of background studies and detection feasibility of selected channels. We conclude in Sec. VI.

II. EFFECTIVE INTERACTIONS

The interactions of the radion with the SM particles on the brane are model-independent and are governed by 4-dimensional general covariance, and thus given by this Lagrangian

$$\mathcal{L}_{\text{int}} = \frac{\phi}{\Lambda_\phi} T_\mu^\mu(\text{SM}), \quad (1)$$

where $\Lambda_\phi = \langle \phi \rangle$ is of order TeV, and T_μ^μ is the trace of SM energy-momentum tensor, which is given by

$$T_\mu^\mu(\text{SM}) = \sum_f m_f \bar{f}f - 2m_W^2 W_\mu^+ W^{-\mu} - m_Z^2 Z_\mu Z^\mu + (2m_h^2 h^2 - \partial_\mu h \partial^\mu h) + \dots, \quad (2)$$

where ... denotes higher order terms. The couplings of the radion with fermions and W , Z and Higgs bosons are given in Eq. (1).

For the coupling of the radion to a pair of gluons (photons), there are contributions from 1-loop diagrams with the top-quark (top-quark and W) in the loop, and from the trace anomaly. The contribution from the trace anomaly for gauge fields is given by

$$T_\mu^\mu(\text{SM})^{\text{anom}} = \sum_a \frac{\beta_a(g_a)}{2g_a} F_{\mu\nu}^a F^{\mu\nu a}. \quad (3)$$

For QCD $\beta_{\text{QCD}}/2g_s = -(\alpha_s/8\pi)b_{\text{QCD}}$, where $b_{\text{QCD}} = 11 - 2n_f/3$ with $n_f = 6$. Thus, the effective coupling of ϕgg , including the 1-loop diagrams of top-quark and the trace anomaly contributions (Fig. 1(a)) is given by

$$\frac{i\delta_{ab}\alpha_s}{2\pi\Lambda_\phi} [b_{\text{QCD}} + y_t(1 + (1 - y_t)f(y_t))] (p_1 \cdot p_2 g_{\mu\nu} - p_{2\mu} p_{1\nu}), \quad (4)$$

where $y_t = 4m_t^2/2p_1 \cdot p_2$ and the momentum and Lorentz index assignments are given in Fig. 1.

The effective coupling of $\phi\gamma\gamma$, including the 1-loop diagrams of the top-quark and W boson, and the trace anomaly contributions (Fig. 1(b)) is given by

$$\frac{i\alpha_{\text{em}}}{2\pi\Lambda_\phi} \left[b_2 + b_Y - (2 + 3y_W + 3y_W(2 - y_W)f(y_W)) + \frac{8}{3}y_t(1 + (1 - y_t)f(y_t)) \right] (p_1 \cdot p_2 g_{\mu\nu} - p_{2\mu} p_{1\nu}), \quad (5)$$

where $y_i = 4m_i^2/2p_1 \cdot p_2$, $b_2 = 19/6$ and $b_Y = -41/6$, and the momentum and Lorentz index assignments are given in Fig. 1. In the above, the function $f(z)$ is given by

$$f(z) = \begin{cases} \left[\sin^{-1} \left(\frac{1}{\sqrt{z}} \right) \right]^2, & z \geq 1 \\ -\frac{1}{4} \left[\log \frac{1+\sqrt{1-z}}{1-\sqrt{1-z}} - i\pi \right]^2, & z < 1 \end{cases}.$$

We now have all necessary couplings to perform calculations on decays and production of the radion.

III. DECAYS OF RADION

With the above interactions we can calculate the partial widths of the radion into $gg, \gamma\gamma, f\bar{f}, WW, ZZ$, and hh . The partial widths are given by

$$\Gamma(\phi \rightarrow gg) = \frac{\alpha_s^2 m_\phi^3}{32\pi^3 \Lambda_\phi^2} |b_{\text{QCD}} + x_t(1 + (1 - x_t)f(x_t))|^2, \quad (6)$$

$$\Gamma(\phi \rightarrow \gamma\gamma) = \frac{\alpha_{\text{em}}^2 m_\phi^3}{256\pi^3 \Lambda_\phi^2} \left| b_2 + b_Y - (2 + 3x_W + 3x_W(2 - x_W)f(x_W)) + \frac{8}{3}x_t(1 + (1 - x_t)f(x_t)) \right|^2, \quad (7)$$

$$\Gamma(\phi \rightarrow f\bar{f}) = \frac{N_c m_f^2 m_\phi}{8\pi \Lambda_\phi^2} (1 - x_f)^{3/2}, \quad (8)$$

$$\Gamma(\phi \rightarrow W^+W^-) = \frac{m_\phi^3}{16\pi \Lambda_\phi^2} \sqrt{1 - x_W} \left(1 - x_W + \frac{3}{4}x_W^2 \right), \quad (9)$$

$$\Gamma(\phi \rightarrow ZZ) = \frac{m_\phi^3}{32\pi \Lambda_\phi^2} \sqrt{1 - x_Z} \left(1 - x_Z + \frac{3}{4}x_Z^2 \right), \quad (10)$$

$$\Gamma(\phi \rightarrow hh) = \frac{m_\phi^3}{32\pi \Lambda_\phi^2} \sqrt{1 - x_h} \left(1 + \frac{x_h}{2} \right)^2, \quad (11)$$

where $x_i = 4m_i^2/m_\phi^2$ ($i = f, W, Z, h$) and $N_c = 3(1)$ for quarks (leptons).

In calculating the partial widths into fermions, we have used the three-loop running masses with scale $Q^2 = m_\phi^2$. Figure 2 shows the branching ratios of the radion up to 1 TeV. Note that the branching ratios are independent of Λ_ϕ . We have also allowed the off-shell decays of the W and Z bosons and that of the top quark, thus giving smooth onset of the WW, ZZ , and $t\bar{t}$ curves. The features of decay branching ratios are similar to the decay of the Higgs boson, except for as follows. At $m_\phi \lesssim 150$ GeV, the decay width is dominated by $\phi \rightarrow gg$ while the decay width of the SM Higgs boson is dominated by the $b\bar{b}$ mode. At larger m_ϕ , ϕ also decays into a pair of Higgs bosons ($\phi \rightarrow hh$) if kinematically allowed while the SM Higgs boson cannot. Similar to the SM Higgs boson, as m_ϕ goes beyond the WW and ZZ thresholds, the WW and ZZ modes dominate with the WW partial width about a factor of two of the ZZ partial width.

IV. PRODUCTION OF RADION

In the following, our discussions are divided according to different colliders, namely, hadron colliders (Tevatron and LHC), lepton colliders ($e^+e^-, \mu^+\mu^-$), and photon colliders.

A. Hadronic colliders

The production channels at hadronic colliders include

$$\begin{aligned} gg &\rightarrow \phi \\ q\bar{q}' &\rightarrow W\phi \\ q\bar{q} &\rightarrow Z\phi \end{aligned}$$

$$\begin{aligned}
qq' &\rightarrow qq'\phi \text{ (} WW, ZZ \text{ fusion)} \\
q\bar{q}, gg &\rightarrow t\bar{t}\phi.
\end{aligned}$$

Similar to the SM Higgs boson, the most important production channel for the radion is gg fusion, which has the lowest order in couplings. In addition, $gg \rightarrow \phi$ gets further enhancement from the anomaly. The production cross section at a hadronic collider with a center-of-mass energy \sqrt{s} is given by

$$\sigma(s) = \int_{m_\phi^2/s}^1 \frac{dx}{x} g(x) g\left(\frac{m_\phi^2}{sx}\right) \frac{\alpha_s^2}{256\pi\Lambda_\phi^2} \frac{m_\phi^2}{s} |b_{\text{QCD}} + y_t(1 + (1 - y_t)f(y_t))|^2, \quad (12)$$

where $g(x)$ is the gluon parton distribution function at momentum fraction x . As shown in Fig. 3, $gg \rightarrow \phi$ has substantially larger cross sections than any other channels for all energies and masses. We shall emphasize using this channel to detect the radion in the next section. We have used the parameterization of CTEQ5L [11] for parton distribution functions.

The associated Higgs production with a vector boson, W or Z , is the golden channel to search for the light Higgs boson at a relatively low energy machine, such as the Tevatron. This is because the W or Z can be tagged to reduce the huge QCD background and Higgs decays mainly into the heaviest flavor $b\bar{b}$. However, for the radion it is not the case because the light radion decays dominantly into gg so that heavy flavor cannot be tagged, but still the associated W or Z boson can be tagged to reduce backgrounds.

The subprocess cross sections for $q\bar{q}' \rightarrow W\phi$ and $q\bar{q} \rightarrow Z\phi$ are given by

$$\begin{aligned}
\hat{\sigma}(q\bar{q}' \rightarrow W\phi) &= \frac{g^2}{192\pi\Lambda_\phi^2} \frac{m_W^4}{(\hat{s} - m_W^2)^2} \sqrt{1 + \frac{(m_W^2 - m_\phi^2)^2}{\hat{s}^2} - \frac{2(m_W^2 + m_\phi^2)}{\hat{s}}} \\
&\times \frac{m_\phi^4 + m_W^4 + 10m_W^2\hat{s} + \hat{s}^2 - 2m_\phi^2(m_W^2 + \hat{s})}{3m_W^2\hat{s}}, \quad (13)
\end{aligned}$$

$$\begin{aligned}
\hat{\sigma}(q\bar{q} \rightarrow Z\phi) &= \frac{g^2(g_L^q{}^2 + g_R^q{}^2)}{96\pi\cos^2\theta_w\Lambda_\phi^2} \frac{m_Z^4}{(\hat{s} - m_Z^2)^2} \sqrt{1 + \frac{(m_Z^2 - m_\phi^2)^2}{\hat{s}^2} - \frac{2(m_Z^2 + m_\phi^2)}{\hat{s}}} \\
&\times \frac{m_\phi^4 + m_Z^4 + 10m_Z^2\hat{s} + \hat{s}^2 - 2m_\phi^2(m_Z^2 + \hat{s})}{3m_Z^2\hat{s}}, \quad (14)
\end{aligned}$$

where $g_{L,R}^f = T_{3f} - Q_f \sin^2\theta_w$ are the chiral $\bar{f}fZ$ couplings, and \hat{s} is the square of the center-of-mass energy of the incoming partons.

The WW and ZZ fusion processes will give an increasing cross section with energy. They are useful production channels at the LHC, especially, when energetic and forward jets are tagged [12] while the other channels would not give rise to energetic nor forward jets. There are a number of subprocesses, e.g., $ud \rightarrow ud\phi$ (WW and ZZ fusion), $uu \rightarrow uu\phi$ (ZZ fusion only), $us \rightarrow dc\phi$ (WW fusion only), etc. Here we only present the formula for the subprocess $ud \rightarrow ud\phi$. The other subprocesses can be obtained from this by removing the interference term and replacing with appropriate chiral couplings. The spin- and color-averaged amplitude-squared for $u(p_1)d(p_2) \rightarrow d(q_1)u(q_2)\phi(k)$ is given by

$$\begin{aligned}
\overline{\sum} |\mathcal{M}|^2 &= \frac{4g^4 m_W^4}{\Lambda_\phi^2} \frac{p_1 \cdot p_2 q_1 \cdot q_2}{[(p_1 - q_1)^2 - m_W^2]^2 [(p_2 - q_2)^2 - m_W^2]^2}, \\
&+ \frac{16g^4 m_Z^4}{\cos^4\theta_w \Lambda_\phi^2} \frac{(g_L^d{}^2 g_R^u{}^2 + g_L^u{}^2 g_R^d{}^2) p_1 \cdot q_1 p_2 \cdot q_2 + (g_L^d{}^2 g_L^u{}^2 + g_R^d{}^2 g_R^u{}^2) p_1 \cdot p_2 q_1 \cdot q_2}{[(p_1 - q_2)^2 - m_Z^2]^2 [(p_2 - q_1)^2 - m_Z^2]^2} \\
&+ \frac{16g^4 m_W^2 m_Z^2}{3\cos^2\theta_w \Lambda_\phi^2} \frac{g_L^d g_L^u p_1 \cdot p_2 q_1 \cdot q_2}{[(p_1 - q_1)^2 - m_W^2] [(p_2 - q_2)^2 - m_W^2] [(p_1 - q_2)^2 - m_Z^2] [(p_2 - q_1)^2 - m_Z^2]}. \quad (15)
\end{aligned}$$

The associated production with a $t\bar{t}$ pair is also nonnegligible because of the large top-quark mass. The formulas for $q\bar{q} \rightarrow t\bar{t}\phi$ and $gg \rightarrow t\bar{t}\phi$ are more complicated and thus presented in the appendix.

The production cross sections for these channels versus the center-of-mass energy and versus m_ϕ are given in Fig. 3(a) and (b), respectively. It is clear that $\sigma(gg \rightarrow \phi)$ is at least two orders of magnitude larger than the other channels. It is only this channel that the production of radion is substantially larger than the production of the Higgs boson, in the case of $\Lambda_\phi = v$. In the next section, we shall study a few decay modes of the radion using this $gg \rightarrow \phi$ production channel.

B. e^+e^- Colliders

At e^+e^- colliders, the radion is produced via

$$\begin{aligned} e^+e^- &\rightarrow Z\phi \quad (\text{Higgs bremsstrahlung}) \\ e^+e^- &\rightarrow \nu\bar{\nu}\phi \quad (WW \text{ fusion}) \\ e^+e^- &\rightarrow e^+e^-\phi \quad (ZZ \text{ fusion}). \end{aligned}$$

The differential cross section for the process $e^+e^- \rightarrow Z\phi$ at a center-of-mass energy \sqrt{s} is given by

$$\frac{d\sigma}{d\cos\theta} = \frac{g^2(g_L^e{}^2 + g_R^e{}^2)}{32\pi\cos^2\theta_w\Lambda_\phi^2} \frac{m_Z^4}{(s-m_Z^2)^2} \left(1 + \frac{(m_Z^2-t)(m_Z^2-u)}{sm_Z^2}\right) \sqrt{1 + \frac{(m_Z^2-m_\phi^2)^2}{s^2} - \frac{2(m_Z^2+m_\phi^2)}{s}}, \quad (16)$$

where $t, u = -\frac{(s-m_Z^2-m_\phi^2)}{2}(1 \mp \alpha\cos\theta)$, and $\alpha = \sqrt{s^2 + m_\phi^4 + m_Z^4 - 2m_Z^2m_\phi^2 - 2m_Z^2s - 2m_\phi^2s}/(s - m_Z^2 - m_\phi^2)$. The angular distribution can be easily integrated to obtain the total cross section

$$\sigma = \frac{g^2(g_L^e{}^2 + g_R^e{}^2)}{32\pi\cos^2\theta_w\Lambda_\phi^2} \frac{m_Z^4}{(s-m_Z^2)^2} \sqrt{1 + \frac{(m_Z^2-m_\phi^2)^2}{s^2} - \frac{2(m_Z^2+m_\phi^2)}{s}} \frac{m_\phi^4 + m_Z^4 + 10m_Z^2s + s^2 - 2m_\phi^2(m_Z^2 + s)}{3m_Z^2s}. \quad (17)$$

There are also contributions from WW and ZZ fusion. The amplitude-squared for WW fusion: $e^-(p_1)e^+(p_2) \rightarrow \nu(q_1)\bar{\nu}(q_2)\phi$, and for ZZ fusion: $e^-(p_1)e^+(p_2) \rightarrow e^-(q_1)e^+(q_2)\phi$, summed over final-state spins and averaged over initial spins are given by

$$\overline{\sum} |M|_{\text{WW}}^2 = \frac{4g^4m_W^4}{\Lambda_\phi^2} \frac{p_1 \cdot q_2 p_2 \cdot q_1}{[(p_1 - q_1)^2 - m_W^2]^2 [(p_2 - q_2)^2 - m_W^2]^2}, \quad (18)$$

$$\overline{\sum} |M|_{\text{ZZ}}^2 = \frac{16g^4m_Z^4}{\cos^4\theta_w\Lambda_\phi^2} \frac{(g_L^e{}^4 + g_R^e{}^4)p_1 \cdot q_2 p_2 \cdot q_1 + 2g_L^e{}^2g_R^e{}^2 p_1 \cdot p_2 q_1 \cdot q_2}{[(p_1 - q_1)^2 - m_Z^2]^2 [(p_2 - q_2)^2 - m_Z^2]^2}. \quad (19)$$

The above three processes at e^+e^- colliders are not particularly different from the corresponding ones of the Higgs boson. Given $\Lambda_\phi = v$ they would be the same. At any rates, the production of these processes are given in Fig. 4(a) and (b) for cross sections versus \sqrt{s} and m_ϕ , respectively.

C. $\gamma\gamma$ Colliders

The radion can be directly produced in $\gamma\gamma$ collisions via the triangular loops of W boson and top quark, as well as the coupling from the trace anomaly of the gauge group. The production cross section at a center-of-mass energy $\sqrt{s_{\gamma\gamma}}$ of $\gamma\gamma$ collision is given by

$$\hat{\sigma} = \frac{\alpha_{\text{em}}^2}{64\pi\Lambda_\phi^2} \frac{s_{\gamma\gamma}}{m_\phi} \delta(\sqrt{s_{\gamma\gamma}} - m_\phi) \left| b_2 + b_Y - (2 + 3y_W + 3y_W(2 - y_W)f(y_W)) + \frac{8}{3}y_t(1 + (1 - y_t)f(y_t)) \right|^2. \quad (20)$$

Nearly monochromatic photon collider is achievable with the technique of laser backscattering [13] on e^+e^- colliders. The unpolarized photon flux resulting from the laser backscattering is

$$f(x) = \frac{1}{D_\xi} \left(1 - x + \frac{1}{1-x} - \frac{4x}{\xi(1-x)} + \frac{4x^2}{\xi^2(1-x)^2} \right), \quad (21)$$

where $D_\xi = (1 - 4/\xi - 8/\xi^2)\log(1 + \xi) + 1/2 + 8/\xi - 1/2(1 + \xi)^2$ and x is momentum fraction of the energy of the incoming electron carried away by the backscattered photon. The choice of $\xi = 4.8$ optimizes the monochromaticity of the photon beam. The production cross sections for radion versus the radion mass for a few linear collider energies are given in Fig. 5.

V. EXPERIMENTAL DETECTION

A. Hadronic Collisions

gg. The most obvious difference in decay modes between the radion and the SM Higgs boson is the $\phi \rightarrow gg$ mode at the low radion mass ($\lesssim 150$ GeV). Other than that the decay modes of the radion with moderate to heavy mass are similar to those of the SM Higgs boson. Here we study the detection of radion using $gg, b\bar{b}, WW$, and ZZ modes.

We first look at the sensitivity to the past and the present experimental data. The UA2 collaboration had searched for particles that decay into a pair of jets in $p\bar{p}$ collisions at $\sqrt{s} = 630$ GeV [14]. Due to low collision energy, they only searched particles of mass between about 100 and 300 GeV. In their searches, they particularly searched for extra W and Z bosons, but the sensitivity for other particles that decay into a pair of jets is similar. On the other hand, the data from CDF [15] give limits on a heavier mass range from 200 GeV to about 1 TeV. They can be combined in the sense that the whole mass range from 100 GeV to 1 TeV is covered.

The UA2 limits on their searches for Z' and W' are shown in Fig. 6. We used a thick line to show the fact that the UA2 studied a number of W' and Z' models and the curves are closely packed together. In Fig. 6, we have used a very small value for $\Lambda_\phi = 100$ GeV, in order to make the radion curve appear on the figure. However, radion production is far below the 90% C.L. upper limits offered by UA2, even for such a small Λ_ϕ .

Similarly, in Fig. 7 we show the dijet production of the radion for mass above 200 GeV, assuming the radion still decays dominantly into gg (though it is not the case as shown in Fig. 2.)[†] But still the radion production is substantially below the 95% C.L. upper limit offered by CDF, even though we used a $\Lambda_\phi = 100$ GeV. The conclusion here is that the present dijet background is far too large for the radion in the dijet mode to be sensitive.

We also investigate the possibility of dijet mode at the LHC. We emphasize the heavy radion with $m_\phi > 1$ TeV and naturally with $\Lambda_\phi \gtrsim 246$ GeV. We show in Fig. 8 the differential cross section versus the dijet invariant mass for the QCD background (we have employed the leading-order calculation) and for the radion signal $gg \rightarrow \phi \rightarrow gg$. Here we have also assumed $B(\phi \rightarrow gg) = 1$ to illustrate the best scenario. We have imposed a strong $p_T(j) > 500$ GeV on each jet, $|\cos\theta^*| < 2/3$, and $|y_j| < 2$ to suppress the QCD background, and employed a smearing of $\Delta E/E = 100\%/\sqrt{E}$ on the jets. We used a bin resolution of 100 GeV and the signals essentially spread into 2 bins (where we have assumed the intrinsic width of the radion is negligible.) In Fig. 8, we see that the signal is about 1–2% of the QCD background in the corresponding bins. Therefore, it is very difficult to identify the signal given such large systematic uncertainties in dijet production. Should we have used a much smaller Λ_ϕ the signal would have been large enough to be identified. However, such a small Λ_ϕ but with a TeV radion mass is rather unnatural.

b \bar{b} . Another possibility is using the $b\bar{b}$ mode of the radion, though the branching ratio is only of order 0.1 whereas the $b\bar{b}$ mode of the SM Higgs boson is close to 1. CDF collaboration [16] has searched for the WH and ZH production and obtained 95% C.L. upper limits on their production. We show the production of $W\phi$ and $Z\phi$ with $\phi \rightarrow b\bar{b}$ and W and Z decay leptonically and hadronically in Fig. 9, where the 95% C.L. upper limit obtained by CDF is also shown. It is clear that only the case with Λ_ϕ much less 100 GeV would it be sensitive to the data. As a consequence, the detection of the radion seems much worse than the SM Higgs boson because of depletion of $b\bar{b}$ mode.

ZZ. Since radion production by gg fusion is substantially larger than the SM Higgs boson, we shall see that using WW and ZZ modes the discovery of the radion is much better than the Higgs boson. For radion heavier than 180 GeV, $\phi \rightarrow ZZ \rightarrow 4l$ is the gold-plated mode. The production is mainly via gluon fusion (see Fig. 3), and the final state would be four charged leptons. We expect this mode remains the gold-plated one for the radion with masses larger than about 180 GeV, as long as the Λ_ϕ and m_ϕ are not getting too large. For illustration we show the invariant mass M_{ZZ} distribution at the 2 TeV Tevatron in Fig. 10 for radion signals with $m_\phi = 200 - 600$ GeV and $\Lambda_\phi = 246$ GeV, together with the background from $q\bar{q} \rightarrow ZZ$ added. The choice of $\Lambda_\phi = 246$ GeV makes the couplings of the radion the same as the SM Higgs boson, except for the gg and $\gamma\gamma$ couplings. We have used an angular cut of $|\cos\theta_Z^*| < 0.8$ on the center-of-mass scattering angle of the Z boson pair. From the figure we can see peak structures for $m_\phi = 200 - 400$ GeV, but only a small bump for $m_\phi > 400$ GeV, and almost no structure for $m_\phi > 600$ GeV. To account for observation we have to take into account the event rate. The four-lepton decay mode of ZZ has a branching ratio of 0.0045. The event rate for $m_\phi = 400$ GeV ($\sigma = 0.032$ pb) is about 4.4 for an integrated luminosity of 30 fb^{-1} (Run IIb) and thus is marginal for discovery. Therefore, any radion heavier than 400 GeV is hard to be detected in Run II. In other words, using $gg \rightarrow \phi \rightarrow ZZ \rightarrow 4l$ the radion with mass upto about 400 GeV would be discovered at RunIIb of the Tevatron.

[†]In Ref. [8], it is shown that in some cases the mixing of the radion and the Higgs boson causes the radion to decay dominantly into gg even for moderate to heavy radion mass.

The situation at the LHC will improve significantly. We show in Fig. 11 the invariant mass M_{ZZ} distribution at the LHC for $\Lambda_\phi = 246$ GeV and 1 TeV. We can see that the signal is way above the background. The detectability depends on event rates and clarity of a peak structure. Since the width of the radion scales as $1/\Lambda_\phi^2$, the peak structure starts to lose when $m_\phi > 800$ GeV for the case of $\Lambda_\phi = 246$ GeV. For $\Lambda_\phi = 1$ TeV, the peak structure of the radion remains even for a 1 TeV radion. The event rate for the 1 TeV radion to decay into four charged lepton is about 39 for $\Lambda_\phi = 1$ TeV, which is more than enough for discovery given such a small background. When Λ_ϕ becomes small we have to take into account the unitarity of the calculation, but we do not concern ourselves with it here. For $\Lambda_\phi = 1$ TeV unitarity should be safe.

WW. A recent study in Ref. [17] showed that the production and decay of the SM Higgs boson in $gg \rightarrow H \rightarrow W^*W^* \rightarrow l\bar{l}\nu$ allows the detection of the Higgs for $145 \lesssim m_H \lesssim 180$ GeV at a 3σ level. For the case of radion, since the production cross section of $gg \rightarrow \phi$ is substantially larger, we expect the detectability of the radion to be significantly better than the Higgs boson. Based on the analysis performed in Ref. [17] we estimate the signal and signal-to-background significance of the radion. The results are shown in Table I. We have used their background numbers and the efficiencies, but with our own cross sections and branching ratios of the radion. We show the results for two choices of $\Lambda_\phi = 0.246$ and 1 TeV. Thus, we can see that if $\Lambda_\phi \approx v$ the radion can be easily identified in the mass range of 140–190 GeV using the W^*W^* decay mode. Even if Λ_ϕ becomes as large as 1 TeV the radion detectability is still better than the SM Higgs boson [17].

TABLE I. Cross sections for the radion signal in the channel $gg \rightarrow \phi \rightarrow W^*W^* \rightarrow l\bar{l}\nu$ and the corresponding significance. The background cross sections are from Ref. [17].

m_ϕ (GeV)	140	150	160	170	180	190
$\Lambda_\phi = 246$ GeV						
σ (fb)	18	28	32	31	28	25
bkgd (fb)	44	30	4.4	2.4	3.8	7.5
S/\sqrt{B} (30 fb ⁻¹)	15	28	83	108	78	18
$\Lambda_\phi = 1$ TeV						
σ (fb)	1.1	1.7	1.9	1.8	1.7	1.5
bkgd (fb)	44	30	4.4	2.4	3.8	7.5
S/\sqrt{B} (30 fb ⁻¹)	0.9	1.7	5.1	6.5	4.8	3.0

B. e^+e^- Colliders

The search strategy for the radion at e^+e^- colliders is very similar to that of Higgs bosons, because the production mechanisms are the same and the decays are similar. The only difference is that for the mass range relevant to LEP search, the dominant decay mode of the radion is $\phi \rightarrow gg$ instead of $b\bar{b}$. Thus, except for heavy flavor tagging, the radion or the Higgs decays into a pair of jets. With b -tagging the effectiveness against backgrounds for finding the Higgs boson is better than the radion. Therefore, the limit on the radion would be lower than the limit on the Higgs boson, if not slightly lower, provided that $\Lambda_\phi = v$. If $\Lambda_\phi > v$ the limit would be worse, and vice versa. The most updated LEP limit on the SM Higgs boson mass is 107.9 GeV [18] using all decay channels of Z and H .

At higher \sqrt{s} , e.g., the next linear collider (NLC) energies, the useful channels include also the WW and ZZ fusion. These production cross sections rise with \sqrt{s} while the H -bremstrahlung mechanism decreases with \sqrt{s} .

So far, we have only studied cases with $\Lambda_\phi \leq 1$ TeV. What will happen to the signal when Λ_ϕ becomes as large as 2 – 3 TeV? The obvious answer is that various signals get smaller because the signal cross sections scale by $1/\Lambda_\phi^2$.

For those dijet channels (jj and $b\bar{b}$) the already huge background will further bury the even smaller signal. For the ZZ channel we have shown that Run II with 30 fb^{-1} integrated luminosity can marginally detect a radion of mass $m_\phi = 400$ GeV and $\Lambda_\phi = 246$ GeV. Therefore, at the Tevatron there is no hope of observing the radion if $\Lambda_\phi \geq 1$ TeV. At the LHC the $ZZ \rightarrow 4\ell$ remains the golden channel for larger Λ_ϕ as long as there are enough signal events. Take $m_\phi = 1$ TeV the background is only about 1.8 events for a mass bin of 100 GeV around 1 TeV. The signal goes down by $1/\Lambda_\phi^2$. Therefore, for $\Lambda_\phi = 3$ TeV the signal event rate goes down to about 4, which may only be marginally enough for discovery. The situation for the WW channel would be similar, though it is not as good as the ZZ channel.

At e^+e^- collider, again the signal cross section scales by $1/\Lambda_\phi^2$. The chance of discovering the radion becomes weaker and weaker when Λ_ϕ gets larger.

VI. CONCLUSIONS

In this work, we have studied the effective interactions, decay, production, and detection of the radion, which is perhaps lighter than the Kaluza-Klein excitations of gravitons in the Randall-Sundrum scenario with the bulk modulus field being stabilized by the Goldberger-Wise mechanism.

The effective interactions of the radion are very similar to the SM Higgs boson, except for the ϕgg and $\phi\gamma\gamma$ couplings, which include the anomaly contribution. Because of the anomalous ϕgg coupling, the dominant decay mode for m_ϕ lighter than about 150 GeV is the gg mode, instead of the $b\bar{b}$ mode. However, once m_ϕ heavier than WW and ZZ thresholds the WW and ZZ modes dominate.

Again, the hadronic production of the radion is dominated by $gg \rightarrow \phi$. The other production channels: WW and ZZ fusion, $W\phi$, $Z\phi$, and $t\bar{t}\phi$ at hadron colliders are just similar to those of the SM Higgs boson. At e^+e^- colliders, the production channels are similar to those of the Higgs bosons.

Although the radion decay is dominated by the gg mode for $m_\phi \lesssim 150$ GeV and the production via $gg \rightarrow \phi$ is anomalously large, this signal $gg \rightarrow \phi \rightarrow gg$ is still buried under the dijet background, as demonstrated in Fig. 6 at $\sqrt{s} = 630$ GeV and in Fig. 7 at $\sqrt{s} = 1.8$ TeV. Similar situation would hold at the LHC. We have also shown that $q\bar{q}' \rightarrow V\phi \rightarrow (l\nu + qq)gg$ is not useful.

On the other hand, we have studied the ZZ and WW decay modes of the radion with the radion produced by $gg \rightarrow \phi$. Based on a study on $H \rightarrow W^*W^* \rightarrow l\bar{\nu}l\nu$ we have shown that the detection of radion is much better than the Higgs boson, because of the anomalously large production of $gg \rightarrow \phi$ (see Table I). The gold-plated mode $\phi \rightarrow ZZ \rightarrow lll$ is the cleanest signature for radion for $m_\phi \gtrsim 180$ GeV. At Run II with a luminosity of 30 fb^{-1} up to $m_\phi = 400$ GeV with $\Lambda_\phi = v$ can be discovered. The situation at the LHC improves significantly. Even with $\Lambda_\phi = 1$ TeV, the radion with mass all the way to 1 TeV can be discovered with a sharp peak. If Λ_ϕ is relatively small, the peak structure becomes a broad bump, but is still much larger than the SM background. We, therefore, urge the experimenters to search for the radion using the ZZ and WW modes.

ACKNOWLEDGMENTS

This research was supported in part by the U.S. Department of Energy under Grants No. DE-FG03-91ER40674 and by the Davis Institute for High Energy Physics, and in part by a grant from the NSC of Taiwan R.O.C.

APPENDIX A:

1. $q\bar{q}, gg \rightarrow t\bar{t}\phi$

Here we present the helicity amplitudes for $q(p_1, j) \bar{q}(p_2, i) \rightarrow t(q_1, k) \bar{t}(q_2, l) \phi(k_1)$, where the momenta and color indices are denoted in the parentheses.

$$i\mathcal{M}_1 = -i \frac{g_s^2 m_t}{\Lambda_\phi} T_{ij}^a T_{kl}^a \frac{1}{(p_1 + p_2)^2} \frac{1}{(q_1 + k_1)^2 - m_t^2} \bar{v}(p_2) \gamma^\mu u(p_1) \bar{u}(q_1) (\not{q}_1 + \not{k}_1 + m_t) \gamma_\mu v(q_2), \quad (\text{A1})$$

$$i\mathcal{M}_2 = -i \frac{g_s^2 m_t}{\Lambda_\phi} T_{ij}^a T_{kl}^a \frac{1}{(p_1 + p_2)^2} \frac{1}{(q_2 + k_1)^2 - m_t^2} \bar{v}(p_2) \gamma^\mu u(p_1) \bar{u}(q_1) \gamma_\mu (-\not{k}_1 - \not{q}_2 + m_t) v(q_2). \quad (\text{A2})$$

There are eight Feynman diagrams contributing to the subprocess $g(p_1, a) g(p_2, b) \rightarrow t(q_1, i) \bar{t}(q_2, j) \phi(k_1)$. They are given by

$$i\mathcal{M}_1 = ig_s^2 (T^a T^b)_{ij} \frac{m_t}{\Lambda_\phi} \frac{1}{(q_1 + k_1)^2 - m_t^2} \frac{1}{(p_2 - q_2)^2 - m_t^2} \bar{u}(q_1) (\not{q}_1 + \not{k}_1 + m_t) \not{p}_1 (\not{p}_2 - \not{q}_2 + m_t) \not{p}_2 v(q_2), \quad (\text{A3})$$

$$i\mathcal{M}_2 = ig_s^2 (T^a T^b)_{ij} \frac{m_t}{\Lambda_\phi} \frac{1}{(q_1 - p_1)^2 - m_t^2} \frac{1}{(p_2 - q_2)^2 - m_t^2} \bar{u}(q_1) \not{p}_1 (\not{q}_1 - \not{p}_1 + m_t) (\not{p}_2 - \not{q}_2 + m_t) \not{p}_2 v(q_2), \quad (\text{A4})$$

$$i\mathcal{M}_3 = ig_s^2 (T^a T^b)_{ij} \frac{m_t}{\Lambda_\phi} \frac{1}{(q_1 - p_1)^2 - m_t^2} \frac{1}{(q_2 + k_1)^2 - m_t^2} \bar{u}(q_1) \not{p}_1 (\not{q}_1 - \not{p}_1 + m_t) \not{p}_2 (-\not{q}_2 - \not{k}_1 + m_t) v(q_2), \quad (\text{A5})$$

$$i\mathcal{M}_4 = ig_s^2 (T^a T^b - T^b T^a)_{ij} \frac{m_t}{\Lambda_\phi} \frac{1}{(p_1 + p_2)^2} \frac{1}{(q_1 + k_1)^2 - m_t^2} \bar{u}(q_1) (\not{q}_1 + \not{k}_1 + m_t) \gamma^\rho v(q_2) \\ \times [(p_1 - p_2)_\rho \epsilon(p_1) \cdot \epsilon(p_2) + 2p_2 \cdot \epsilon(p_1) \epsilon(p_2)_\rho - 2p_1 \cdot \epsilon(p_2) \epsilon(p_1)_\rho], \quad (\text{A6})$$

$$i\mathcal{M}_5 = ig_s^2 (T^a T^b - T^b T^a)_{ij} \frac{m_t}{\Lambda_\phi} \frac{1}{(p_1 + p_2)^2} \frac{1}{(q_2 + k_1)^2 - m_t^2} \bar{u}(q_1) \gamma^\rho (-\not{q}_2 - \not{k}_1 + m_t) v(q_2) \\ \times [(p_1 - p_2)_\rho \epsilon(p_1) \cdot \epsilon(p_2) + 2p_2 \cdot \epsilon(p_1) \epsilon(p_2)_\rho - 2p_1 \cdot \epsilon(p_2) \epsilon(p_1)_\rho], \quad (\text{A7})$$

$$i\mathcal{M}'_1 = i\mathcal{M}_1 [(p_1, a) \leftrightarrow (p_2, b)], \quad (\text{A8})$$

$$i\mathcal{M}'_2 = i\mathcal{M}_2 [(p_1, a) \leftrightarrow (p_2, b)], \quad (\text{A9})$$

$$i\mathcal{M}'_3 = i\mathcal{M}_3 [(p_1, a) \leftrightarrow (p_2, b)], \quad (\text{A10})$$

where $\epsilon(p_i)$'s denote the polarization 4-vectors for the gluons.

- [1] N. Arkani-Hamed, S. Dimopoulos, and G. Dvali, Phys. Lett. **B429**, 263 (1998); I. Antoniadis *et al.*, Phys. Lett. **B436**, 257 (1998).
- [2] K. Cheung, talk presented at PASCOS'99, Granibakken, Tahoe, CA, December 1999, hep-ph/0003306.
- [3] K. Dienes, E. Dudas, and T. Gherghetta, Nucl. Phys. **B537**, 47 (1999).
- [4] L. Randall and R. Sundrum, Phys. Rev. Lett. **83**, 3370 (1999); *ibid.* **83**, 4690 (1999).
- [5] W. Goldberger and M. Wise, Phys. Rev. Lett. **83**, 4922 (1999).
- [6] W. Goldberger and M. Wise, Phys. Lett. **B475** 275 (2000).
- [7] C. Csáki, M. Graesser, L. Randall, and J. Terning, Phys. Rev. **D62**, 045015 (2000); C. Csáki, M. Graesser, and G. Kribs, hep-th/0008151.
- [8] G. Giudice, R. Rattazzi, and J. Wells, hep-ph/0002178.
- [9] U. Mahanta and A. Datta, Phys. Lett. **B483** 196 (2000); U. Mahanta and S. Rakshit, Phys. Lett. **B480** 176 (2000).
- [10] S. Bae, P. Ko, H. Lee, and J. Lee, Phys. Lett. **B487** 299 (2000).
- [11] CTEQ Coll. (H.L. Lai *et al.*), Eur. Phys. J. **C12**, 375 (2000).
- [12] V. Barger *et al.*, Phys. Rev. **D44**, 1426 (1991).
- [13] V. Telnov, Int. J. Mod. Phys. **A13**, 2399 (1998).
- [14] UA2 Coll., J. Alitti *et al.*, Z. Phys. **C49**, 17 (1991); Nucl. Phys. **B400**, 3 (1993).
- [15] CDF Coll., Phys. Rev. **D55**, 5263 (1997).
- [16] CDF Coll., Phys. Rev. Lett. **81**, 5748 (1998).

[17] T. Han, A. Turcot, and R. Zhang, Phys. Rev. **D59**, 093001 (1999).

[18] "Search for Higgs bosons: preliminary combined results using LEP data collected at energies up to 202 GeV", LEP working group, CERN-EP-2000-055.

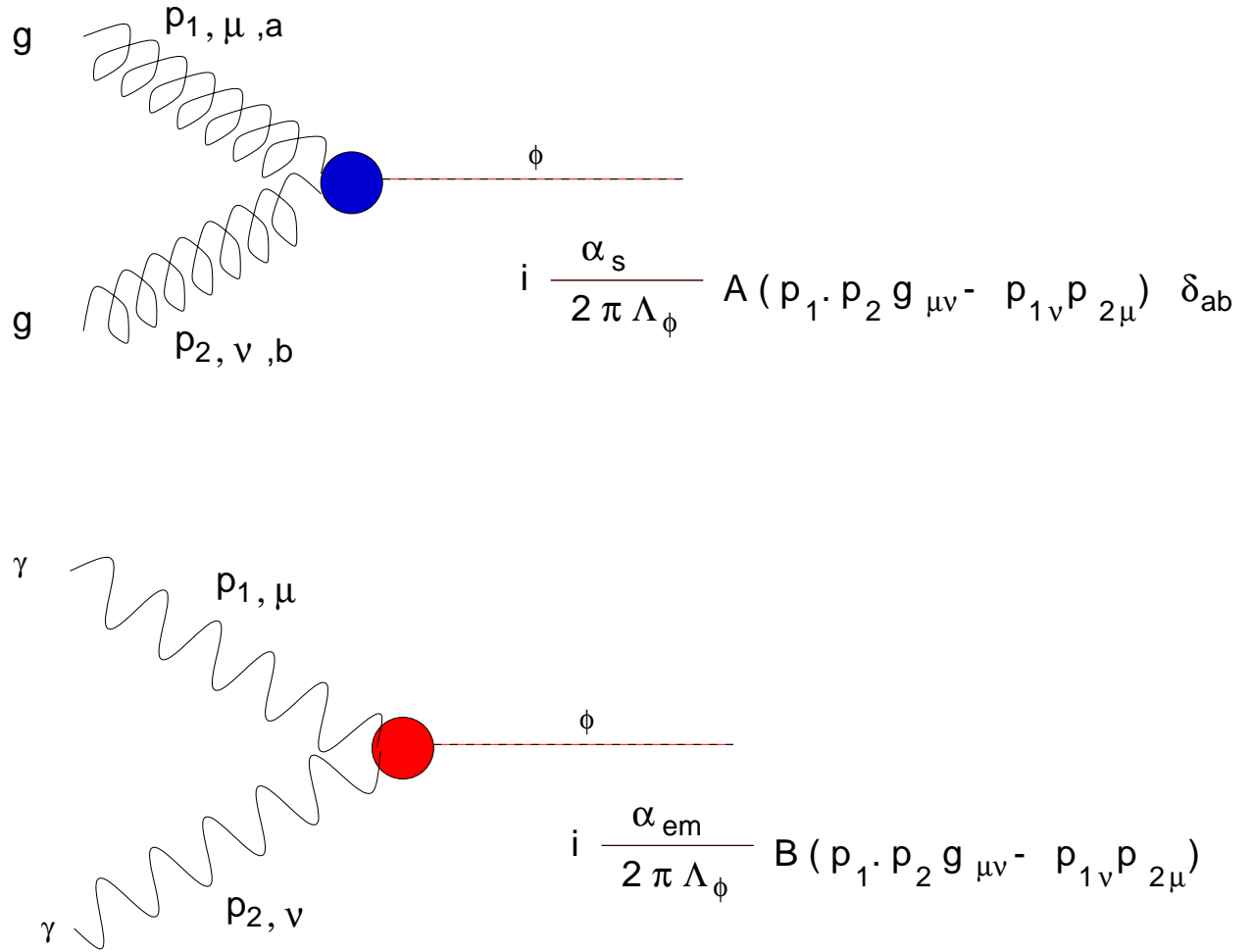


FIG. 1. Feynman diagrams and rules for (a) $gg\phi$ vertex and (b) $\gamma\gamma\phi$ vertex. The constant $A = b_{\text{QCD}} + y_t(1 + (1 - y_t)f(y_t))$ and $B = b_2 + b_Y - (2 + 3yw + 3yw(2 - yw)f(yw)) + \frac{8}{3}y_t(1 + (1 - y_t)f(y_t))$, where $y_i = 4m_i^2/2p_1 \cdot p_2$. a and b are color indices of the gluons.

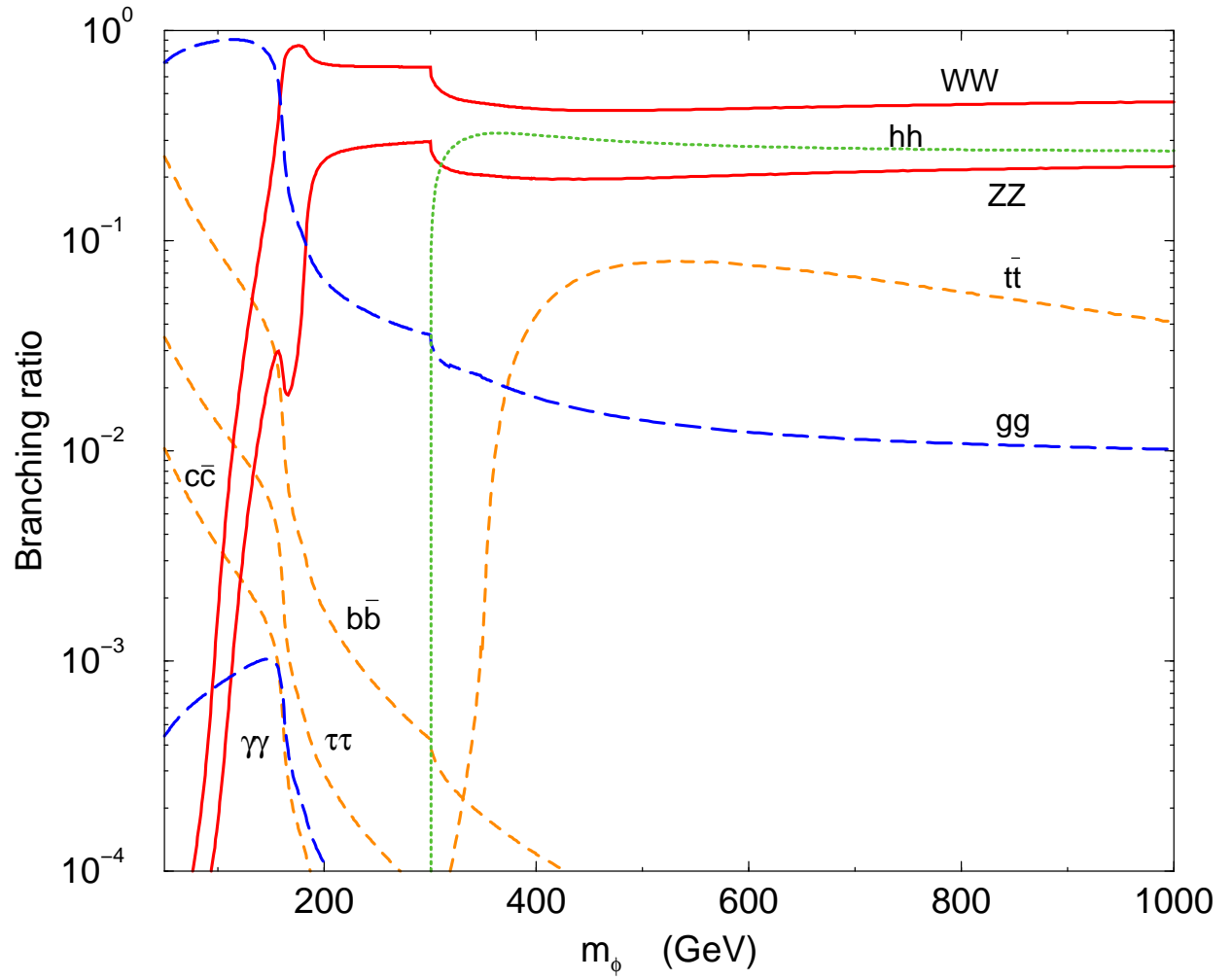


FIG. 2. Branching ratios of the radion versus m_ϕ . Here we have used $m_h = 150$ GeV.

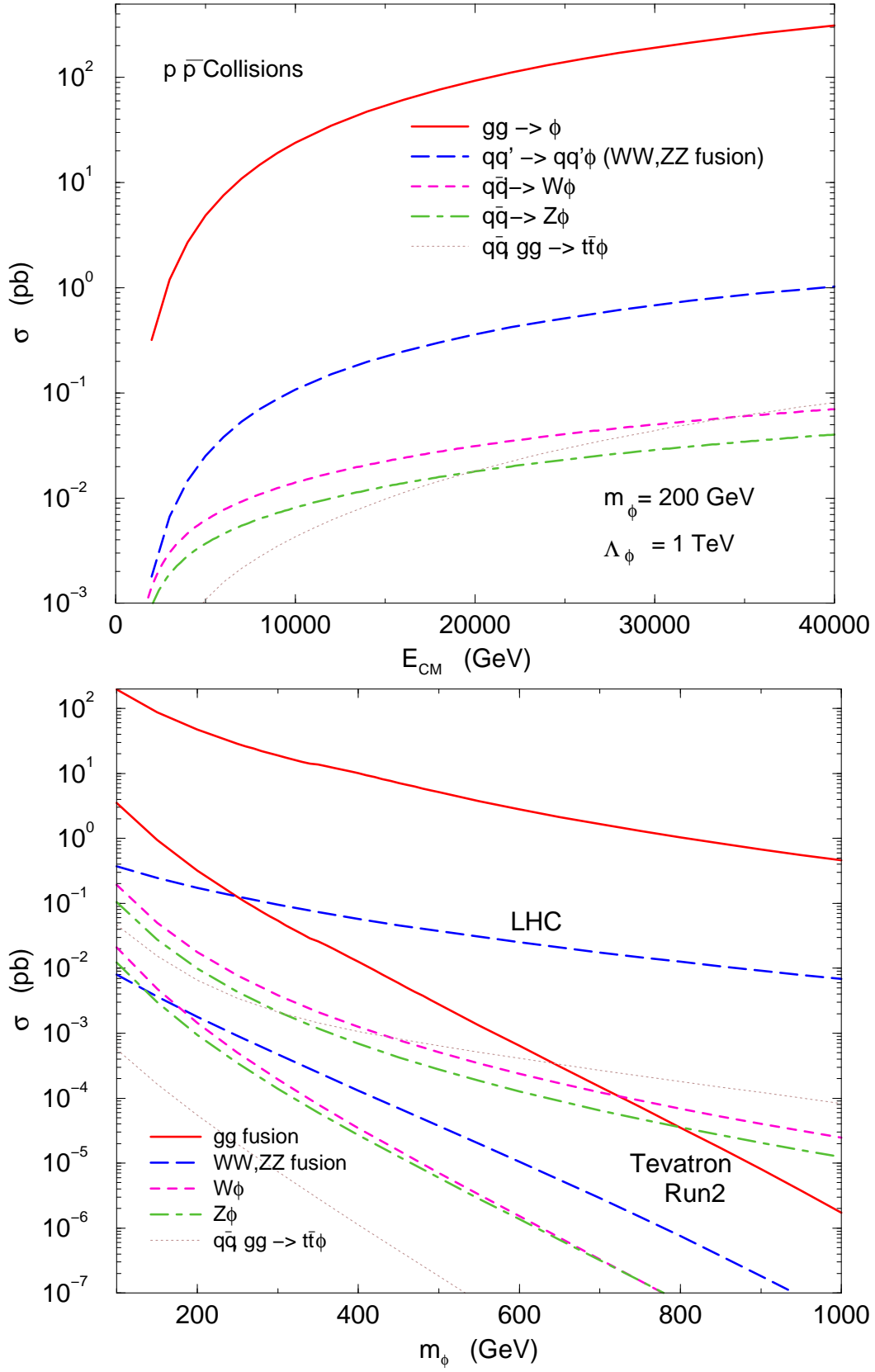


FIG. 3. (a) Production cross sections versus the center-of-mass energy E_{CM} for $p\bar{p} \rightarrow \phi$ (gg fusion), $p\bar{p} \rightarrow qq'\phi$ (WW, ZZ fusion), $p\bar{p} \rightarrow W\phi$, $p\bar{p} \rightarrow Z\phi$, and $p\bar{p} \rightarrow t\bar{t}\phi$. (b) Production cross sections versus m_ϕ .

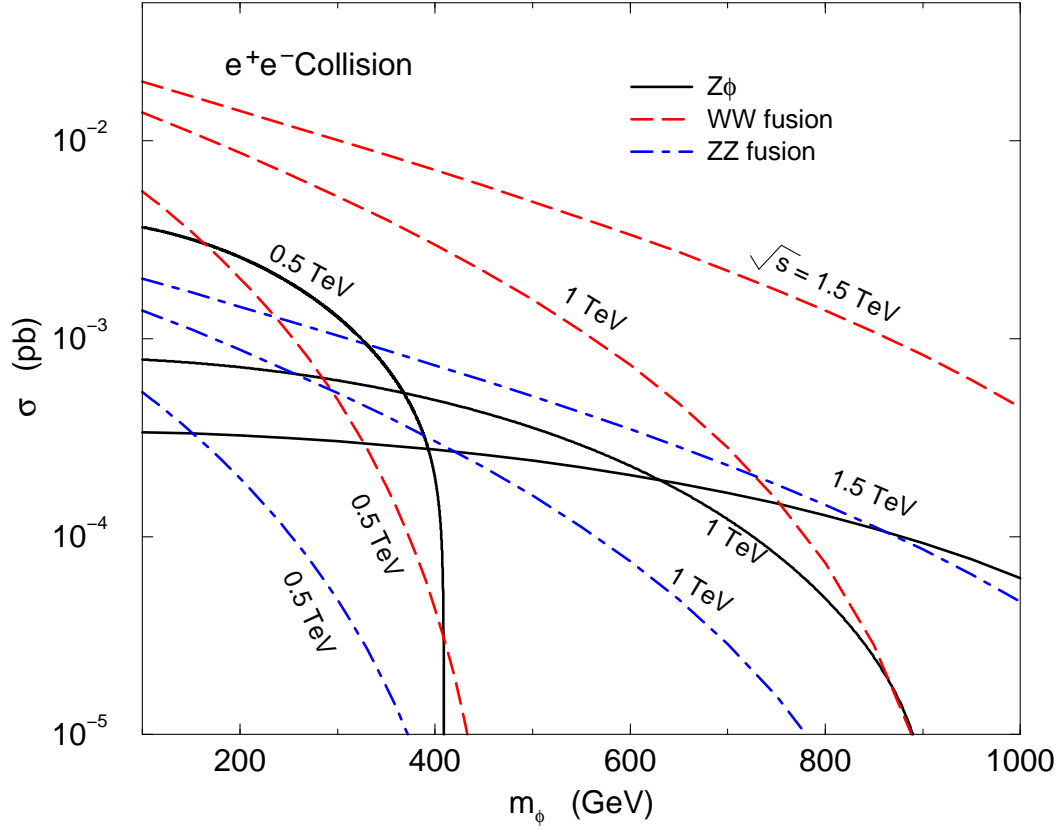
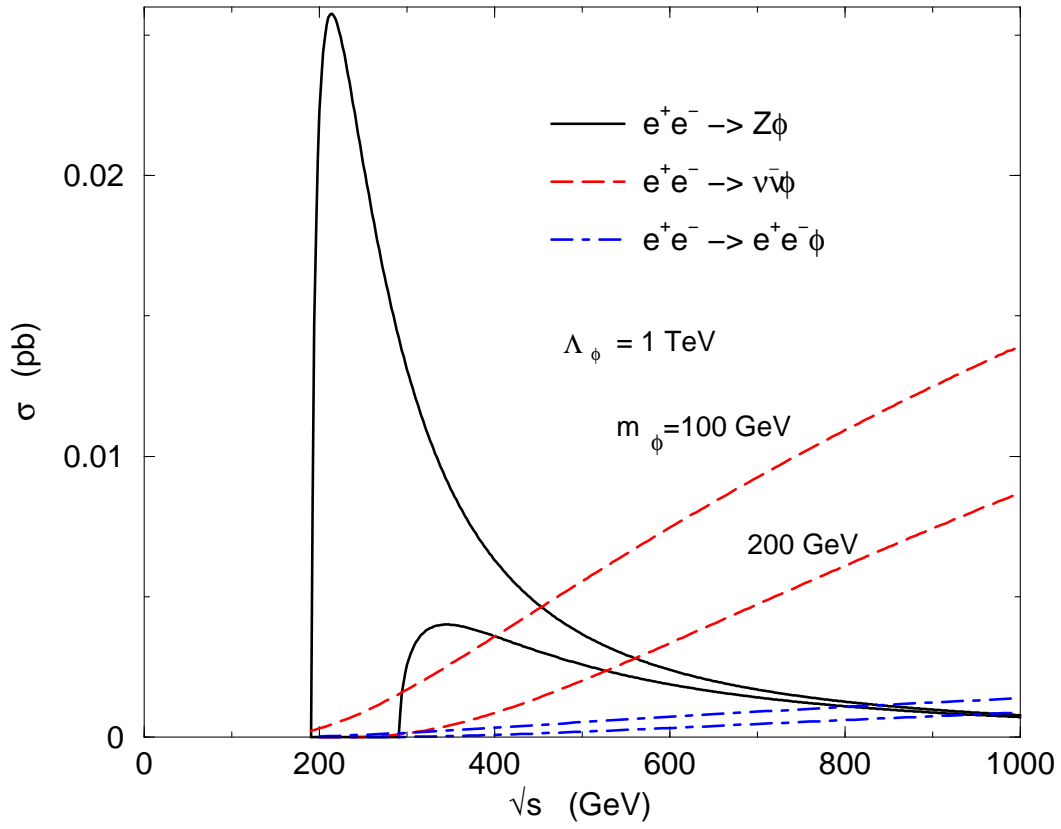


FIG. 4. (a) Production cross sections versus the center-of-mass energy \sqrt{s} for $e^+e^- \rightarrow Z\phi$, $e^+e^- \rightarrow \nu\bar{\nu}\phi$ (WW fusion), and $e^+e^- \rightarrow e^+e^-\phi$ (ZZ fusion). (b) Production cross sections versus m_ϕ .

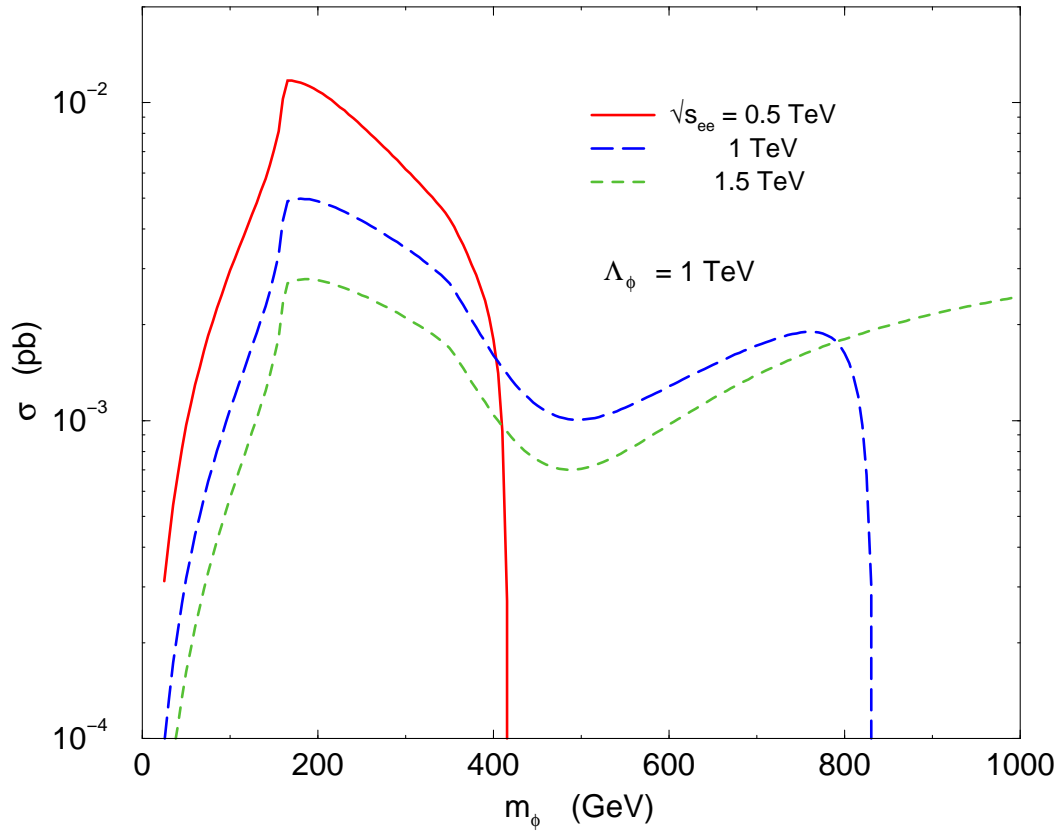


FIG. 5. Production cross sections for the radion versus m_ϕ at linear e^+e^- colliders in the backscattering $\gamma\gamma$ mode.

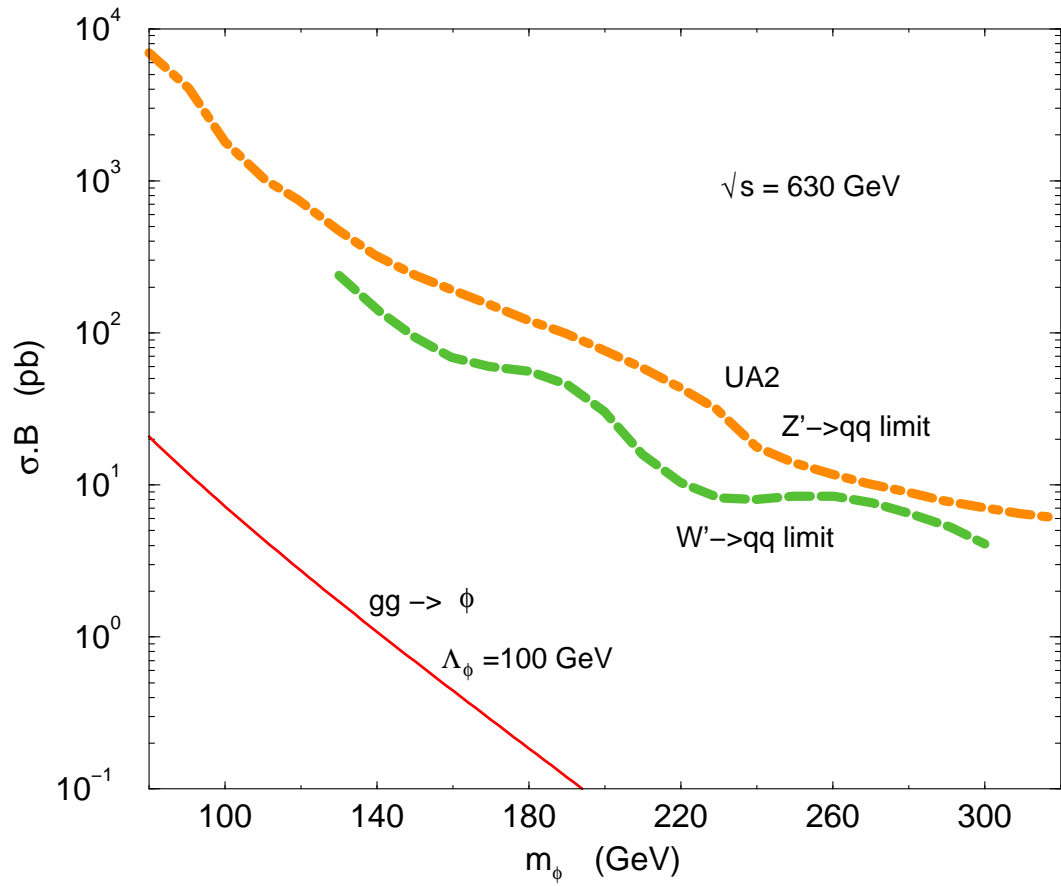


FIG. 6. Dijet production cross section for the radion using $gg \rightarrow \phi$ channel at $\sqrt{s} = 630$ GeV, assuming $B(\phi \rightarrow gg) = 1$. The UA2 90% C.L. upper limits on dijet production from decays of heavy bosons (Z' and W') are shown.

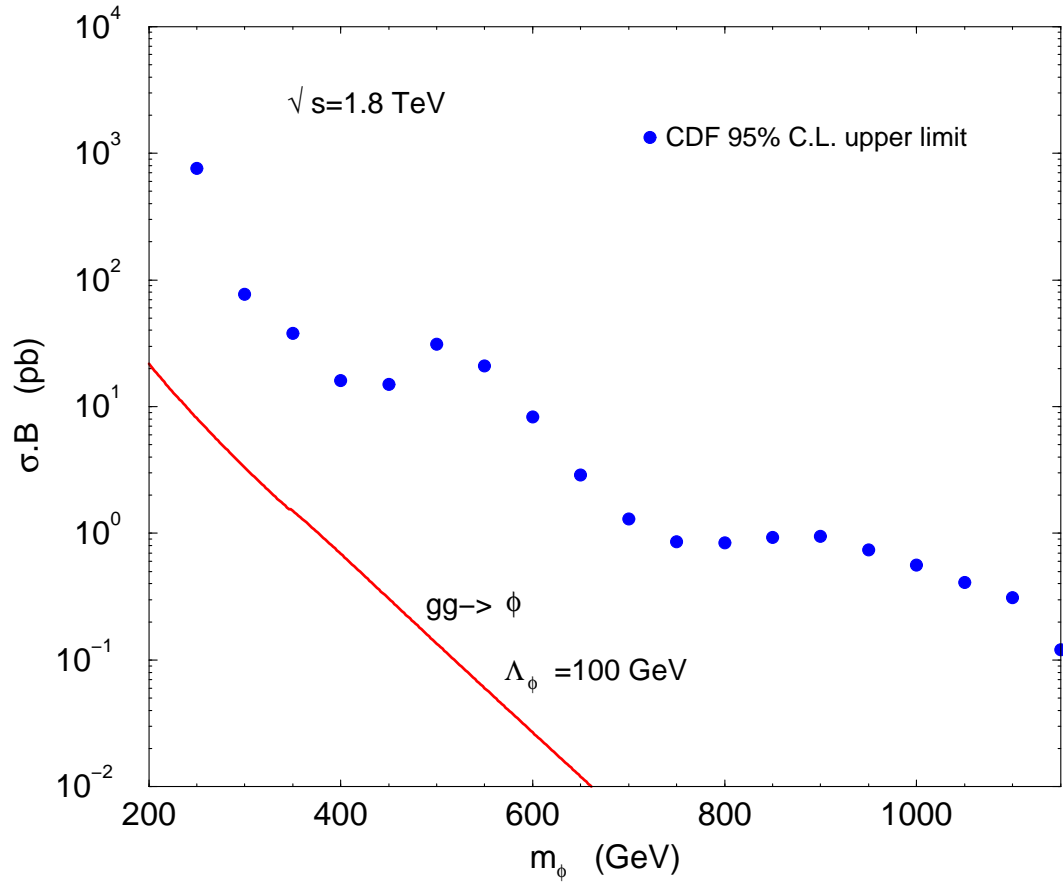


FIG. 7. Dijet production cross section for the radion using $gg \rightarrow \phi$ channel at $\sqrt{s} = 1.8$ TeV, assuming $B(\phi \rightarrow gg) = 1$. The CDF 95% C.L. upper limit on dijet production from the decay of a new particle is shown.

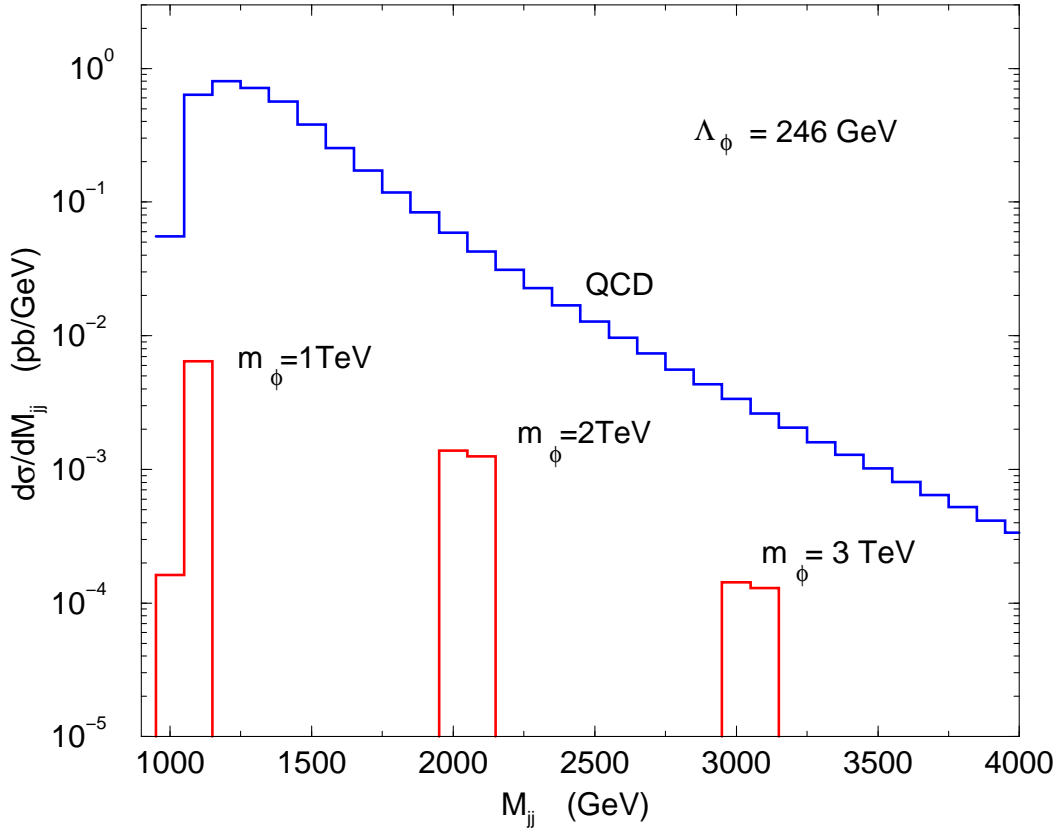


FIG. 8. Differential cross section versus dijet invariant mass for the QCD background and for radion signals (1–3 TeV) using $gg \rightarrow \phi \rightarrow gg$ at the LHC. We have assumed $B(\phi \rightarrow gg) = 1$. We have imposed a strong $p_T(j) > 500$ GeV on each jet, $|\cos \theta^*| < 2/3$ and $|y_j| < 2$, and employed a smearing of $\Delta E/E = 100\%/\sqrt{E}$ on the jets.

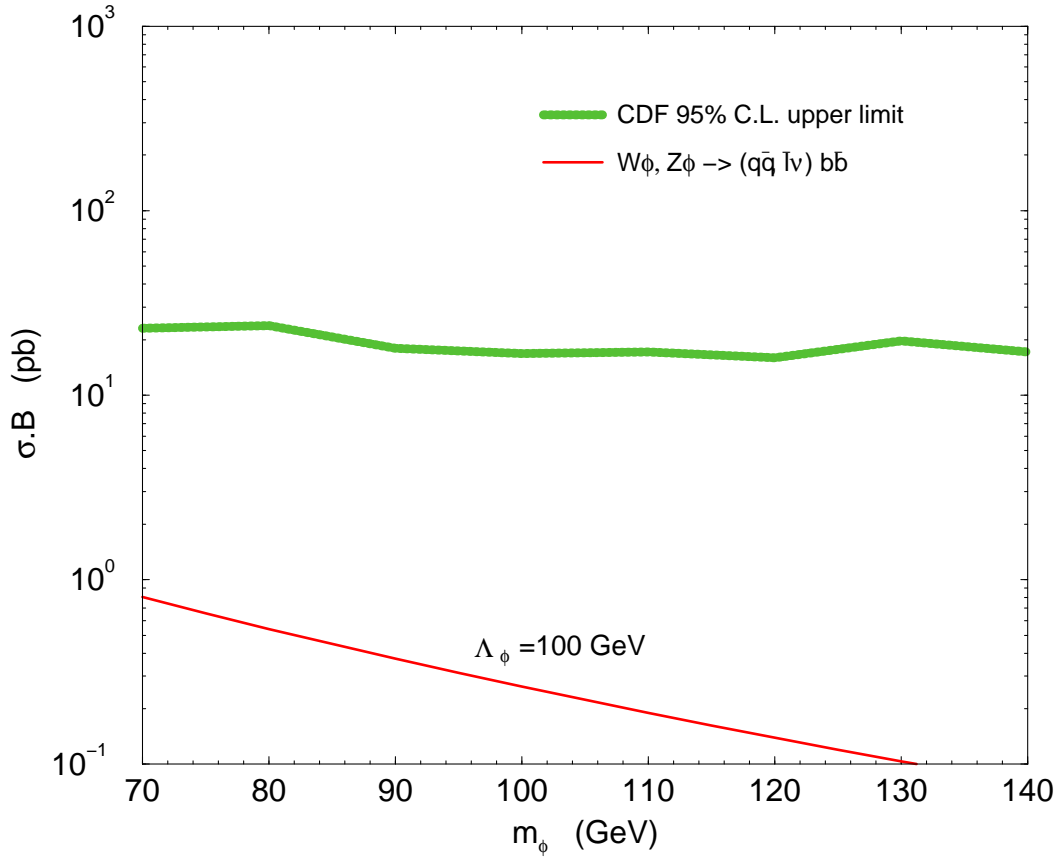


FIG. 9. Cross section for the radion production using $p\bar{p} \rightarrow V\phi \rightarrow (q\bar{q} + l\nu)b\bar{b}$ ($V = W, Z$) at $\sqrt{s} = 1.8$ TeV, assuming $B(\phi \rightarrow b\bar{b}) = 0.1$. The CDF 95% C.L. upper limit on $VH^0 \rightarrow (q\bar{q} + l\nu)b\bar{b}$ is shown.

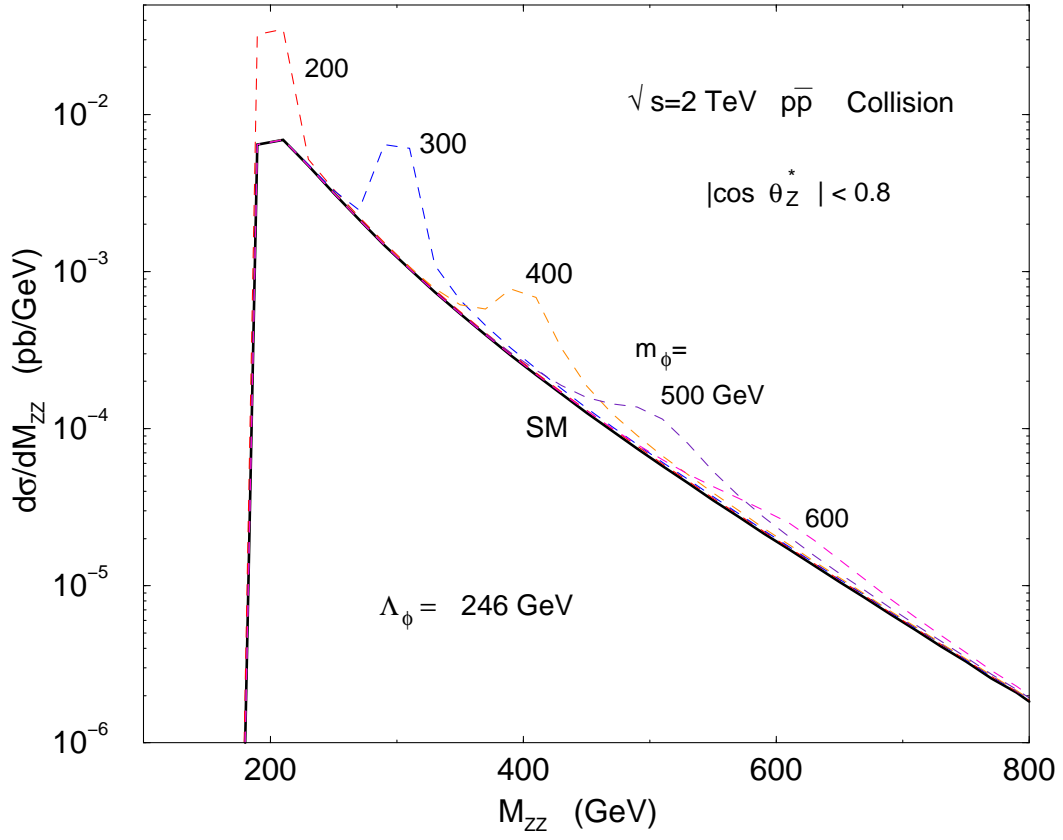


FIG. 10. Invariant mass distribution $d\sigma/dM_{ZZ}$ for the radion signal with $m_\phi = 200 - 600$ GeV and the SM background $q\bar{q} \rightarrow ZZ$ at $\sqrt{s} = 2$ TeV $p\bar{p}$ collision, for $\Lambda_\phi = 246$ GeV. A cut of $|\cos \theta_Z^*| < 0.8$ is imposed.

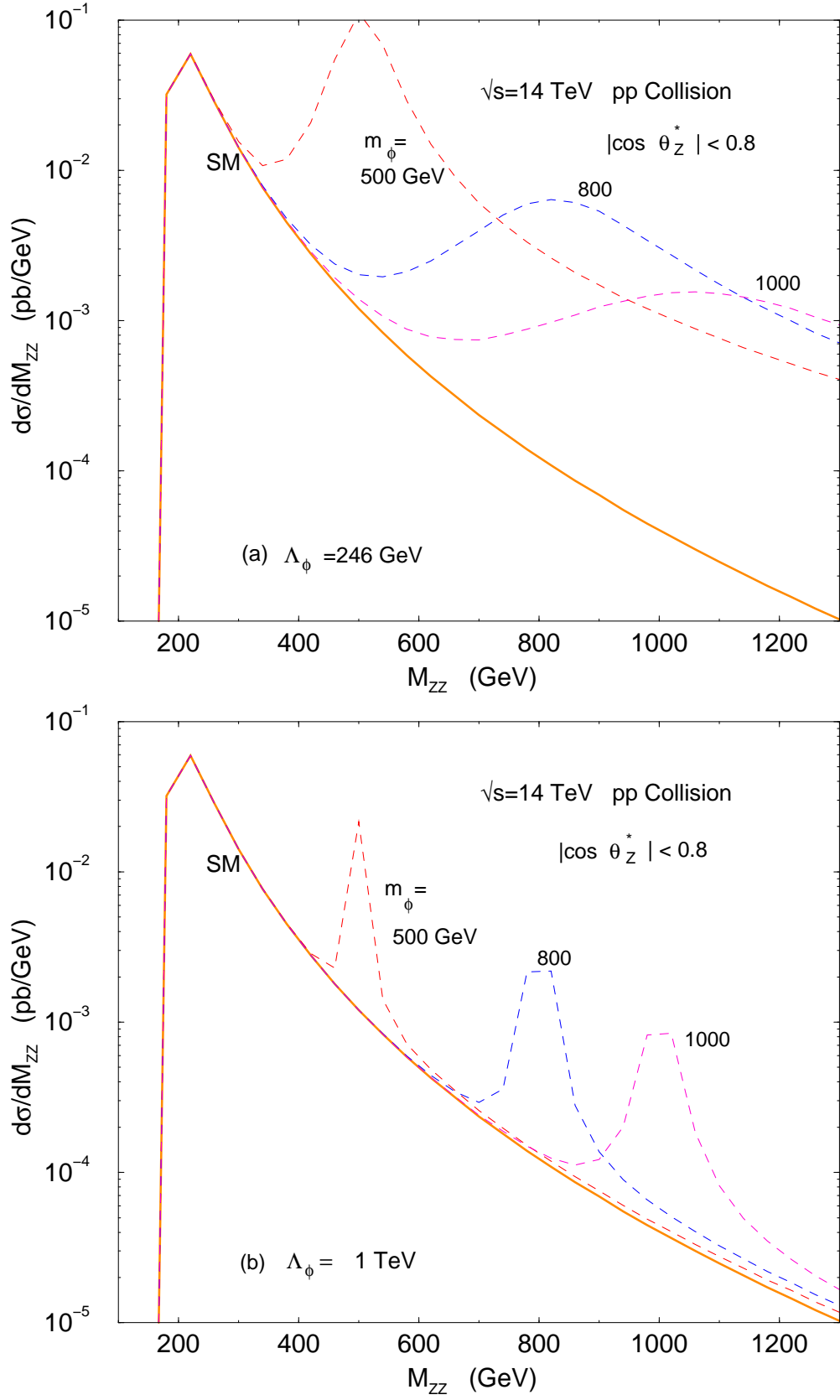


FIG. 11. Invariant mass distribution $d\sigma/dM_{ZZ}$ for the radion signal with $m_\phi = 500, 800, 1000$ GeV and the SM background $q\bar{q} \rightarrow ZZ$ at the LHC, for (a) $\Lambda_\phi = 246$ GeV and (b) $\Lambda_\phi = 1$ TeV. A cut of $|\cos \theta_Z^*| < 0.8$ is imposed.